Progress In Electromagnetics Research B, Vol. 30, 83–102, 2011

A 3D MODEL TO CHARACTERIZE HIGH-FREQUENCY SCATTERING BY URBAN AREAS FOR MONOSTATIC AND BISTATIC RADAR CONFIGURATIONS

N. T. M. Nguyen, D. Lautru, and H. Roussel

UPMC Univ Paris 06
UR2 L2E, F-75252, Paris, France

Abstract—In this paper, we propose a 3D model to characterize the field scattered by an urban area, which is composed of a group of buildings, for both monostatic and bistatic radar configurations. This model is based on a ray-tracing technique combined with the Uniform Theory of Diffraction (UTD). It is useful not only in elucidating mechanisms of ray propagation through the observed area, but also in evaluating the amplitude and the phase of any point in the far-zone scattered field above the ground. In order to validate the model, some comparisons with the commercial software XGTD® are presented. In addition, our model is tested against 33–37 GHz indoor measurements conducted in the anechoic chamber of the "ElectroMagnetic Effects Research Lab" (EMERL) in Singapore. These latter comparisons have shown that the model can predict precisely the location of a target placed between two metallic plates representing walls.

1. INTRODUCTION

Synthetic Aperture Radar (SAR) imaging of urban areas has received much interest in recent years with some promising applications [1–3]. A major challenge is to give a fast and accurate ElectroMagnetic (EM) model in order to provide synthetic data for imaging algorithms. The faster the information retrieval process, the more effective the actions to reach required objectives. Moreover, in a way to evaluate the best bistatic radar configuration, it is necessary, at the beginning, to develop a three-dimensional model to predict the diffracted field by a scenario.

Received 8 March 2011, Accepted 4 May 2011, Scheduled 6 May 2011
Corresponding author: Ngoc Truong Minh Nguyen (minhn2t@yahoo.com).

This information can be employed for many uses such as infrastructure development planning, physical environment protection, and traffic surveillance. Many models have been proposed for the propagation prediction in urban medium [4–6].

Due to this issue, a bistatic EM model used to determine the scattered field by an urban area is developed in this paper. A ray-tracing approach with particular attention on multiple wall reflections and diffractions compounding with the high-frequency asymptotic methodology Uniform Theory of Diffraction (UTD) [7, 8] is used to calculate the scattered field. The main advantage of the UTD method is that each completed ray path from the source to the observer corresponds to a physical scattering mechanism, such as reflection (R), diffraction (D), double reflections (R-R), reflection-diffraction (R-D), etc. To illustrate this principle, comparisons between our model and the commercial software XGTD® [9] are likened. Furthermore, some anechoic chamber measurements are conducted to demonstrate the suitability and efficacy of our model for building scattering. This model is validated in the frequency range 33–37 GHz, but can be applied in X-band. It allows us to evaluate at any point in the far-zone the total complex electric field diffracted by a group of buildings. The main objective of the present paper is to characterize the scattered field from the transmitter to the receiver according to urban parameters (shape of buildings, density of buildings, ...). In the second step, we will evaluate with our model the optimal radar configuration for urban applications like area mapping or detection of moving targets.

The paper is outlined as follows. In Section 2, we describe the model beginning from the radar configuration, then the geometrical representation of an urban area. After that, we present the ray-tracing technique combined with the UTD method used to generate the scattered field. In Section 3, we present some comparisons to validate our model both with the commercial software XGTD® and experimental results. Some simulations and interpretations of the scattered field for one building (with flat or inclined roof) or many buildings in a realistic urban area are described in Section 4. Finally, in Sections 5 and 6, we summarize and conclude this paper.

2. THE MODEL

2.1. Radar Configuration

The radar configuration used in our model is illustrated in Fig. 1. The transmitter and the receiver are co-localized or separated in order to perform monostatic or bistatic configurations. (θ_i,ϕ_i) are the elevation

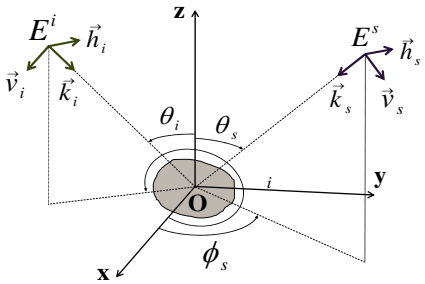

Figure 1. Bistatic scattering configuration.

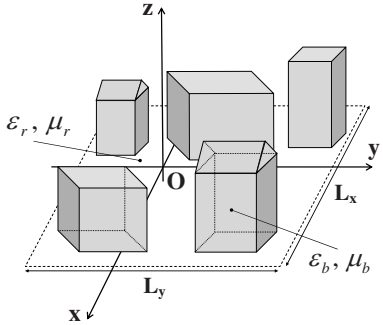

Figure 2. Representation of an $L_x \times L_y$-side urban area.

and azimuth angles of the incident wave; $(\vec{k_i},\vec{v_i},\vec{h_i})$ is the polarization base for the incident wave. We keep the same definition for the scattering wave. This configuration is taken into consideration with the purpose of improving the radar capacity of detection and identification, and thus to increase the detection capability of a target [10, 11].

2.2. Geometrical Representation of Urban Areas

The backscattered fields from urban areas are dominated by multiple reflections from building walls, roofs, and diffractions from building edges. A canonical representation of urban areas including the effects related to the reflections and diffractions is chosen. Indeed, this representation is justified because in the frequency band of interest, the elements composing of urban areas (buildings, cars, ...) are always much more larger than the incident wavelength. Furthermore, the roughness of the ground is not taken into account because it is small compared to the incident wavelength. Buildings are depicted by parallelepipeds with flat or inclined roofs placed at deterministic positions on a dielectric $L_x \times L_y$-side plane representing the air-ground interface (see Fig. 2). The permittivities of the buildings and the ground depend on the building compositions and the soil moisture. They are defined by the real and imaginary parts of its complex relative permittivities ϵ_b and ϵ_r. The relative permeabilities of the buildings μ_b and the ground μ_r are equal to one.

2.3. Ray-tracing

A ray-tracing algorithm is used to determine the geometrical paths of rays inside the illuminated area. Rays are first traced from the

source points to the project. When they intercept building facets or the ground, they are specularly reflected and continue to be delineated up to the maximum number of reflections which is defined in advance or when they hit the study area boundary. However, in order to integrate all the diffraction effects on the building edges where the field becomes discontinuous, the intervals between rays should be reduced and as a consequence increase computing time. To avoid it, we develop a hybrid ray-tracing method which can refine the ray mesh with the aim of including diffraction effects due to the edges of buildings. This adaptive subdivision adjusts the distance between two adjacent rays following different paths through the geometry (i.e., they intercept two different buildings or two adjacent sides of a building, it means that we can generate a tertiary ray between the two previous ones which might be intercepted by an edge). A pre-defined criteria of diffraction is needed when we use this method.

Examples of how the rays launched from the source points on the transmitter used to identify diffracting edges are shown in Fig. 3. If we consider two adjacent rays number 1 and 2, the ray number 1 is reflected by facet 1 while the other is reflected by facet 6. This means that there exists a diffracting edge lying between these two rays. It is accordingly quite simple to locate a diffraction point on the edge and then to construct the path followed by the incident field. Another situation is shown for the two other rays number 3 and 4. These two rays hit the same building but different facets (facets 10 and 9), so a diffracting edge should be situated between them.

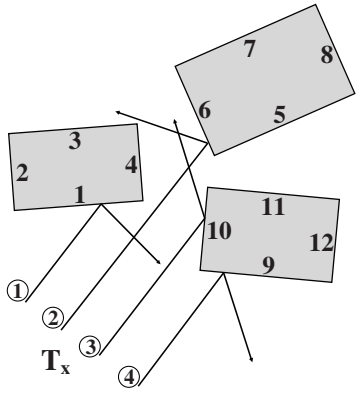

Figure 3. Identifications of the rays intercepting diffracting edges.

2.4. Calculation of the Scattered Field

2.4.1. Reflected Field

Considering a reflection at a point O, the reflected field at a point M (after reflection) is obtained as the sum of two components, vertical and horizontal to the reflection plane, which are functions of the transmitted field, the reflection coefficients and the propagation delay. If we assume that the harmonic time dependence is $e^{j\omega t}$, the reflected field is then given by:

$$\begin{pmatrix} E_v^r(M) \\ E_h^r(M) \end{pmatrix} = \begin{pmatrix} R_v & 0 \\ 0 & R_h \end{pmatrix} \begin{pmatrix} E_v^i(O) \\ E_h^i(O) \end{pmatrix} e^{-j\vec{k}\cdot O\vec{M}} \tag{1}$$

where R_v, R_h are the Fresnel vertical and horizontal reflection coefficients. Thus,

$$\vec{E}^r(M) = E_v^r(M)\vec{v_r} + E_h^r(M)\vec{h_r} \tag{2}$$

2.4.2. Diffracted Field

In the case of a diffraction at a point O (the intersection of a ray with a building edge), the formulation of the diffracted field at a point M (after diffraction) is expressed by using the UTD and given by:

$$\begin{pmatrix} E_v^d(M) \\ E_h^d(M) \end{pmatrix} = \begin{pmatrix} D_v & 0 \\ 0 & D_h \end{pmatrix} \begin{pmatrix} E_v^i(O) \\ E_h^i(O) \end{pmatrix} \frac{e^{-j\vec{k}\cdot O\vec{M}}}{\sqrt{\left|\left|O\vec{M}\right|\right|}} \tag{3}$$

where D_v, D_h are the heuristic vertical and horizontal UTD coefficients of diffraction. Thus,

$$\vec{E}^d(M) = E_v^d(M)\vec{v_d} + E_h^d(M)\vec{h_d} \tag{4}$$

Finally, the total electric field at a given point M (the receiver) will be obtained after some mechanisms of multiple reflections or diffraction(s)-reflection(s) or reflection(s)-diffraction(s). In this study, we take into account only the first order of diffraction, for higher order diffraction, we consider that the signal is weak enough to be neglected. However, the number of reflections can be modified.

3. VALIDATION

To validate the model, we firstly compare it with the commercial software XGTD® and later with a set of measurements in the anechoic chamber.

3.1. Comparisons with the Software XGTD®

In this part, we confront respectively the reflected and diffracted fields calculated by our model and the software. All the comparisons have been done for both vertical and horizontal polarizations.

3.1.1. Reflected Field

The calculated amplitude and phase of vertical and horizontal reflection components for two materials (concrete and soil which have different relative permittivities) with respect to the incident angle are compared to the results obtained by XGTD®. The comparisons give a good agreement in both amplitude and phase (which are not shown in this paper).

3.1.2. Diffracted Field

A simple configuration (see Fig. 4) is conceded for validation. It consists of a right-angled wedge ($\alpha = 90°$) illuminated perpendicularly to its edge by an incident plane wave. The wedge is perfectly conducting or dielectric (concrete of relative permittivity $\epsilon_r = \epsilon'_r - j * 60\sigma\lambda$ where in the computations, relative dielectric permittivity $\epsilon'_r = 7.3$ and conductivity $\sigma = 0.2\,\mathrm{S/m}$). The operating frequency is 10 GHz. The diffracted angle ϕ varies from 0° to 270°. The diffracted field is calculated at points placed on an arc of radius 3 m from the tip of wedge. Once again, the comparisons between our model and the software are in good agreement for both polarizations and materials. However, in the case of an incident angle $\phi' = 120°$ for the dielectric wedge, there are some small discrepancies for both, vV- and hH-, polarizations between our computed results and those from XGTD®. These divergences come from that the diffraction coefficients are calculated according to different references. (See Fig. 5 for an incident angle $\phi' = 45°$ and Fig. 6 for an incident angle $\phi' = 120°$).

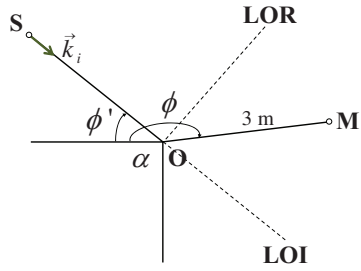

Figure 4. Configuration used for diffraction comparisons.

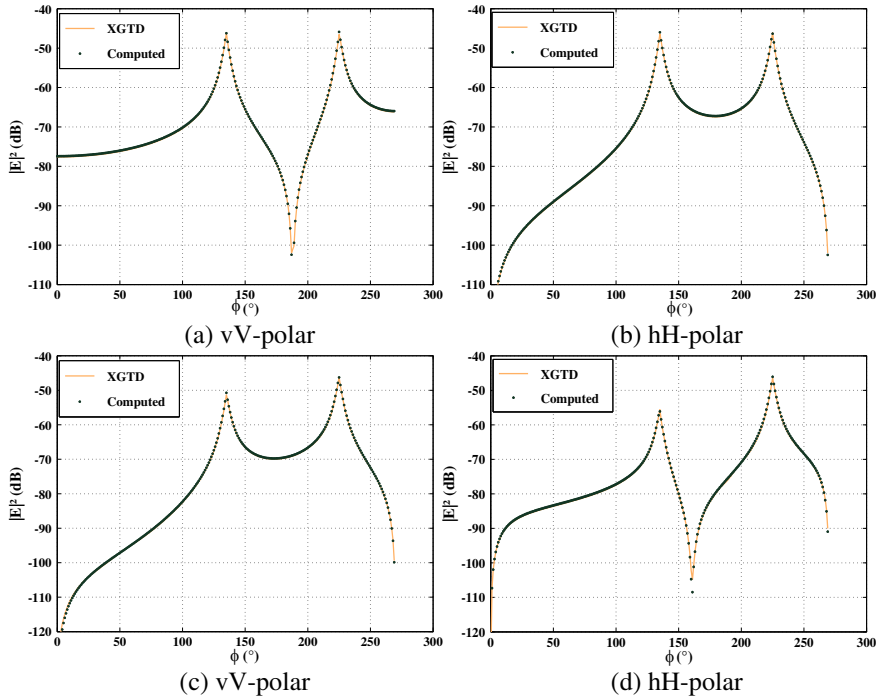

Figure 5. Diffraction on a (a)(b) metallic (c)(d) concrete wedge for an incident angle $\phi' = 45°$, $f = 10\,\text{GHz}$.

Note that vV-polar means the transmitter is vertically polarized (V) while the receiver is in vertical polarization (v).

3.2. Comparisons with Measurements

To better demonstrate the pertinence of the UTD ray-tracing approach in urban areas, we have done some measurements in anechoic chamber for the sake of comparing with our model. Three comparisons consisting of two metallic walls with or without target are considered. The targets are a 4-in-1 (the right-angled size is 10.2 cm) and a 1-in-1 corner reflector (CR) (the right-angled size is 8.0 cm) (see Fig. 7). Two identical BBHA 9170 broadband horn antennas 14–40 GHz are used as the transmitter and the receiver. The total half-power beam-width of the antenna is $13° \times 15°$. In all cases, they are put side-by-side at a height of 2 m upon the ground and both are vertically polarized. The slope angle between the normal of the antennas and the ground is 18°. The working frequency band is from 33 to 37 GHz with a step of 5 MHz. The direct path between two antennas which corresponds to the cable

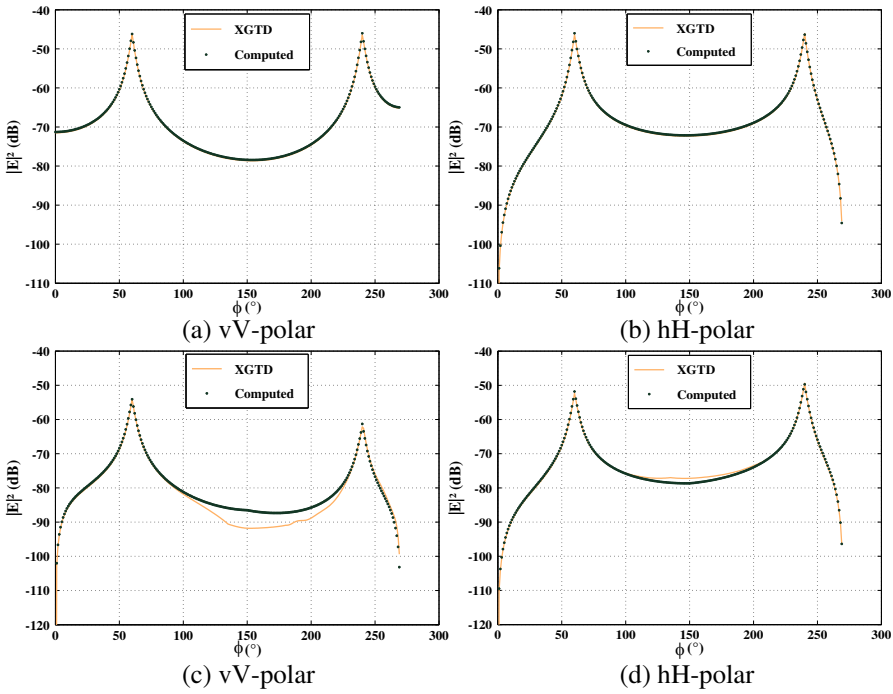

Figure 6. Diffraction on a (a)(b) metallic (c)(d) concrete wedge for an incident angle $\phi' = 120°$, $f = 10\,\text{GHz}$.

length is 1.62 m.

In each case, we compare the measured and simulated range profiles in order to retrieve the distances from the antennas to the walls and the target. At the beginning, the transmitter emits all the incident rays from its main lobe to the project which contains two walls only or with target. We define the maximum number of reflections on the walls, the ground and/or the target up to twenty and only one diffraction on the walls (it should be noted that we do not consider the diffraction on the edges of the targets). Finally, a limited number of rays is intercepted by the receiver (only in the main antenna lobe) after some interactions. Each received ray is characterized by its three complex electric field components E_x, E_y and E_z. These components are then projected on two polarizations of the receiver, vertical (v) and horizontal (h). By the fact that when we change the operating frequency, rays undergo the same interactions, except the phase of the field will be changed. Hence, we consider each case for only one frequency (we choose here 35 GHz) and then we vary the frequency to get different phases. After all, an Inverse Discrete Fourier Transform

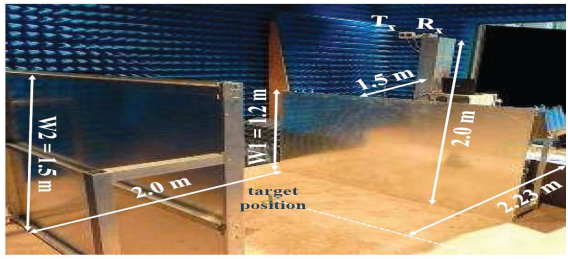

(a)

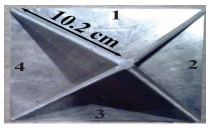

(b)

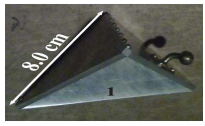

(c)

Figure 7. The configuration of indoor measurements. (a) The sizes of two metallic plates and their relative positions to the antennas. (b) The 4-in-1 corner reflector. (c) The 1-in-1 corner reflector.

(IDFT) is used to get the amplitude of the range profile. The distances in the range profile are calculated by:

$$range\ (m) = (1 : numel(f)) * dr + 1.62 \tag{5}$$

where $f = 33 : 0.005 : 37$ and $dr = c/(2Df) = 3 \cdot 10^8/(2 \cdot (37 - 33) \cdot 10^9) = 0.0375$ m).

In the first case, two metallic plates of heights 1.2 m and 1.5 m are put at 1.5 m and 3.5 m respectively from the antennas as in Fig. 7(a). The comparison between the measured and simulated range profiles obtained for this configuration is shown in Fig. 8. Note that we succeed in retrieving all the peaks obtained by measurements. The first two peaks (number 1 and 2) correspond to the direct diffractions from wall 1 and wall 2. The next five peaks numbered 4, 6, 8, 10 and 12 are due to multiple bounces between two walls (equivalent to 4, 6, 8, 10 and 12 reflections) (see Table 1). For example, the first peak stands for the direct diffraction from the transmitter to the wall 1 and backwards to the receiver as shown in Fig. 9. The distance between the antennas and the top of the first wall is 1.72 m, added to 1.62 m cable length so that in the range profile it appears at the distance of 1.72+1.62 = 3.34 m. The other peaks are obtained in the same way. We observe here a significant difference in magnitude between simulations and measurements. This is due to two reasons: the first is that we have not treated the antenna side lobes because they increase considerably the computation time and secondly is the non-canonical shape of the walls and the target (i.e., the metallic bars attached to the wall plates can cause undesired effects on the received field).

Table 1. Comparison between the positions of the peaks due to multi-reflection on walls, measured and calculated.

Peak number	(1)	(2)	(4)	(6)	(8)	(10)	(12)
Interaction index	001	001	400	600	800	1000	1200
Measurement (m)	3.45	5.25	7.61	9.53	11.48	13.42	15.41
Computing (m)	3.38	5.21	7.50	9.41	11.36	13.35	15.34

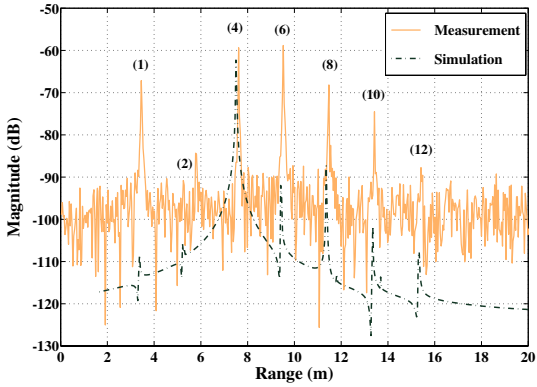

Figure 8. Measured and simulated range profiles for the first case.

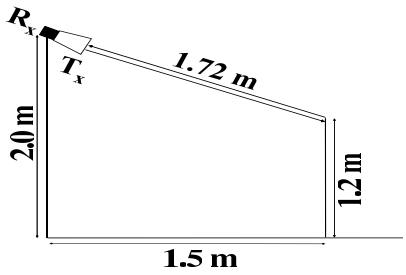

Figure 9. The example of the first peak retrieval in the range profile.

For the second case, we place a 4-in-1 CR, as shown in Fig. 7(b), between two walls at the position of 2.23 m from the antennas. The open angle 1 of the CR is towards to the second wall. In this case, besides all the effects appearing in the first configuration, we have some more interactions corresponding to the target. They have the interaction indices 230, 430, 630, 830, 1030 (see Table 2) and correspond to peak numbers 3, 5, 7, 9 and 11 in Fig. 10. For better understanding, an index "430" means that the ray undergoes four times

of reflections on the walls, three times of reflections on the target and no diffraction as shown in Fig. 11. These five peaks are the results of the reflections on the walls and on the two open angle 1 and 3 of

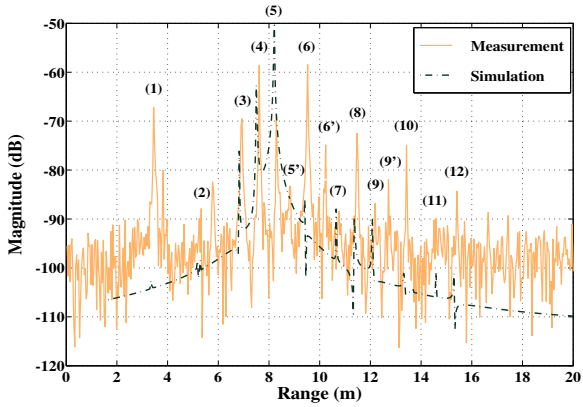

Figure 10. Measured and simulated range profiles for the second case.

Table 2. Comparison of the multi-bounces (on 4-in-1 CR) peaks' ranges between the measurement and computing.

Peak number Interaction index	(3) 230	(5) 430	(7) 630	(9) 830	(11) 1030
Measurement (m)	6.94	8.29	10.76	12.19	14.59
Computing (m)	6.83	8.21	10.65	12.08	14.59

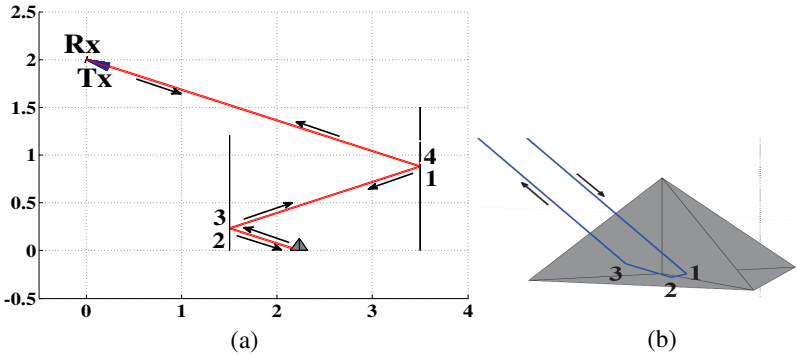

Figure 11. The view of a ray undergoing four times of reflections on the walls, three times of reflections on the target and no diffraction. (a) The side view. (b) Target reflections.

the CR. More precisely, the indices 230, 630 and 1030 are relevant to the open angle 1 while the two others 430 and 830 are due to the opposite open angle. Besides that, there exists three indices 421, 621 and 821 corresponding to peaks 5′, 6′ and 9′. Nevertheless, there is only a few number of received rays associated to these interactions so their amplitudes are too small to be detected as in measurements.

For the third configuration, we change only the target to a 1-in-1 CR in order to identify the peaks due to the previous target (see Fig. 7(c)). The open angle 1 of the CR is towards to the second wall. Unlike the preceding case, we do not observe in Fig. 12 the interactions indices 430 and 830 because of the target shape which does not show up on is the backside of the trihedral (see Table 3). Once again, the same explication as the previous case is conducted to explain the appearances of two peaks 5′ and 9′. Then again, as a consequence of the target shape, the peak number 6′ is not observed in this case.

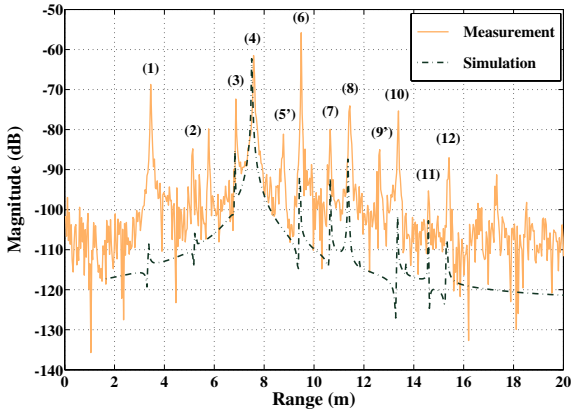

Figure 12. Measured and simulated range profiles for the third case.

Table 3. Comparison of the multi-bounces (on 1-in-1 CR) peaks′ ranges between the measurement and computing.

Peak number	(3)	(7)	(11)
Interaction index	230	630	1030
Measurement (m)	6.86	10.65	14.59
Computing (m)	6.83	10.65	14.59

4. SIMULATIONS

In this section, we want to evaluate the effects of urban parameters (such as building shape, building density, ...) on the far-zone scattered field. The radar configuration for all cases of simulation is illustrated in Fig. 13. The transmitter is characterized by a rectangular aperture representing an incident plane wave illuminating a limited urban area. In order to get a full view of the observed area, what we are interested in is the spot of the incident wave on the ground which should entirely illumine the study scenario. According to this reason, the size of the transmitter depends on each simulation. Furthermore, the transmitter is placed at a height of 700 m upon the ground and the incident angles are ($\theta_i = 30°$, $\phi_i = 45°$). The receiver is a pixel of 1 m × 1 m square aperture moving on a half-sphere of radius 5000 m centred at the origin point O. The transmitted electric field is fully polarized and its amplitude is 1 V/m. The frequency of interest is 10 GHz. The building relative permittivity is that of concrete and is equal to $\epsilon_b = 7.3 - j*0.36$. For the ground, we choose $\epsilon_r = 28.5 - j*12.84$ corresponding to moist soil.

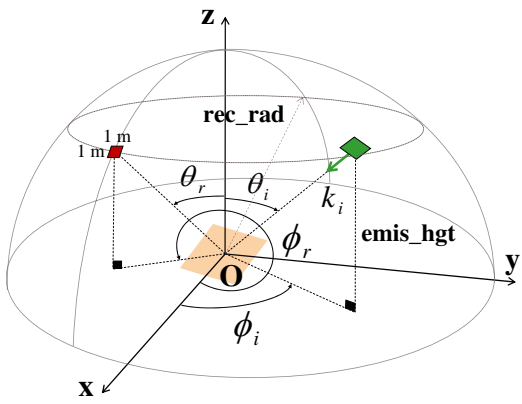

Figure 13. The radar configuration for the simulation.

It should be noted that there are two reasons preventing us from using XGTD® to simulate the full urban model with our hereabove configuration. The first reason is that we cannot remove the incident field out off the study zone to obtain only the scattered field by the observed area. Secondly, each incident ray in XGTD® does not have the same phase reference. The latter reason makes it quite impossible to sum up the total scattered field by a full urban area. This fact enforces the opportunity to present our purposely developed scattering

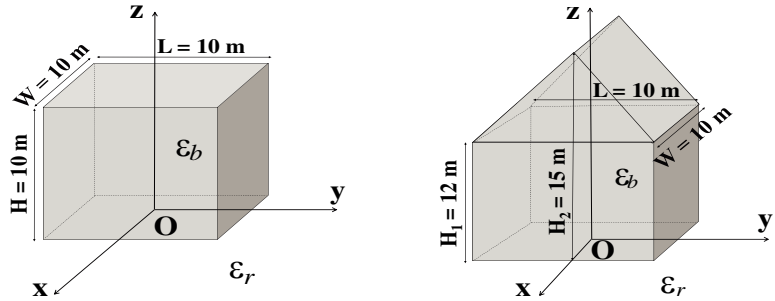

Figure 14. Two buildings with (a) a flat roof (b) an inclined roof.

model.

4.1. Dependence on the Shape of the Building

Let us consider two typical building shapes with flat and inclined roof separately. The dimensions of the building with a flat roof are 10 m × 10 m × 10 m while the building with an inclined roof are 10 m × 10 m × 12 m × 15 m (see Fig. 14). The size of the transmitter in this case is $14m \times 14m$ to fully illuminate the building. The hV-polar corresponds to the vertical polarized transmitter (V) and the horizontal polarized receiver (h).

In the Figs. 15 and 16, the power of the diffracted field in two cases of building shape is presented, for co-polarizations (vV and hH) and cross-polarizations (hV and vH), in the same range from −150 dBm to 0 dBm. Firstly, we can observe the diffractions on the edges of building walls for both co-polarized cases (the line obtained when $\theta_r = \theta_i = 30°$). These diffraction effects are quite weak in the cases of cross-polar. On the other hand, the two parabolic curves in the case of a flat-roof building correspond to the diffractions on the edges between the roof and the walls. For an inclined-roof building, one of these curves is deformed because of the roof shape and the other parabolic curve appears due to the diffractions on the ridge of the roof and its parallel edges.

Moreover, we can also find that there are some particular directions where the scattered fields are stronger than the others. The maxima for co-polarized configurations in both cases of building are obtained in the directions:

- direction 1 ($\theta_r = 30°$, $\phi_r = 225°$) for both cases (specular reflection on the ground),

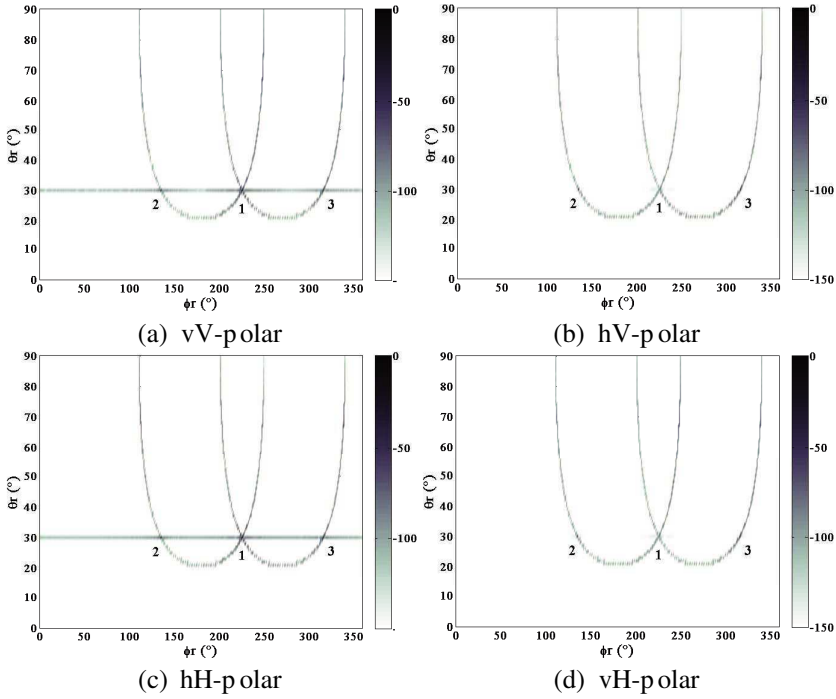

Figure 15. (a)(c) Co- and (b)(d) Cross-polar of the received field for a flat-roof building.

- direction 1 ($\theta_r = 30°$, $\phi_r = 225°$) in the case of a flat-roof building or direction 4 ($\theta_r = 43°$, $\phi_r = 121°$) and 5 ($\theta_r = 84°$, $\phi_r = 249°$) in the case of an inclined-roof building (single reflection on the roof),
- direction 2 ($\theta_r = 30°$, $\phi_r = 135°$) and 3 ($\theta_r = 30°$, $\phi_r = 315°$) for both cases (double reflections wall-ground and ground-wall).

In the cases of cross-polarization, the reflection effects are lower than for co-polarizations. However, the directions where the scattered fields are the most significant are still the same. In general, we notice that the power is higher for co-polarized cases.

4.2. Dependence on the Density of the Buildings

We consider now two configurations including four and twelve buildings. In the first case, the urban area is composed of four buildings. Their heights, lengths and widths are respectively $H = [12\ 14\ 10\ 15]$ (m), $L = [5\ 6\ 7\ 8]$ (m) and $W = [6\ 7\ 7\ 6]$ (m) (see Fig. 17(a)).

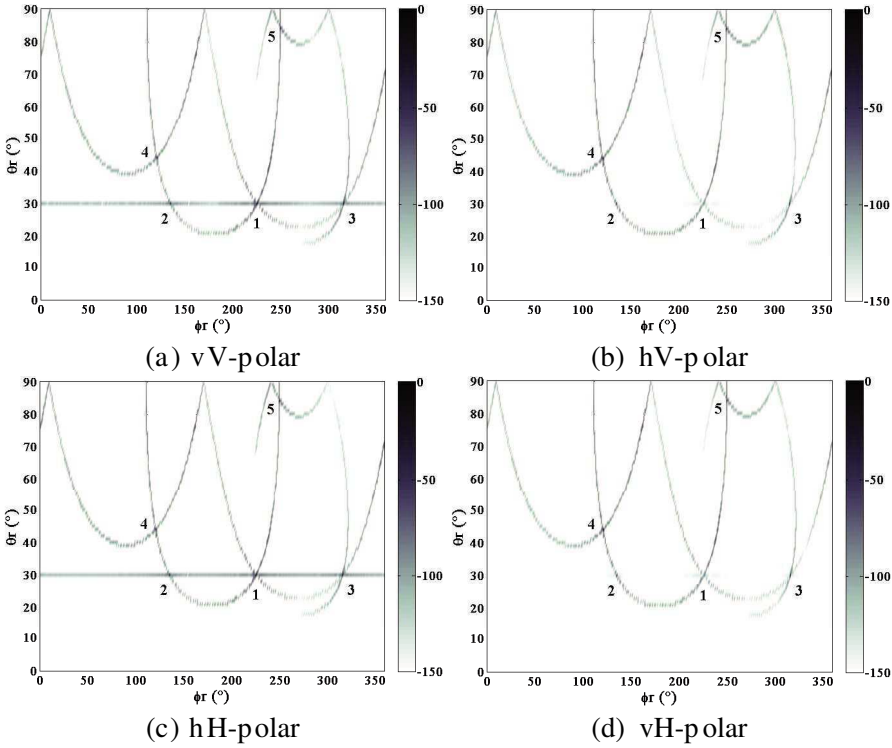

Figure 16. (a)(c) Co- and (b)(d) Cross-polar of the received field for an inclined-roof building.

The transmitter size becomes now a 30 m × 30 m rectangular aperture in a way to illuminate the four buildings.

Figure 18 presents the received power of the diffracted field for all cases of polarizations. It is obviously that the level of the diffracted field for cross-polar is lower than that for co-polar particularly in the direction where we observe the diffraction effects on the edges of building walls. The main contributions come from the field due to multiple reflections because the level of the diffracted rays is much more smaller. Furthermore, there are some directions where the field is stronger, this is due to reflections on the roofs, walls and ground. The maximum is found in the specular direction ($\theta_r = 30°$, $\phi_r = 225°$). Besides that, the continuous parabolic curves are due to the direct diffractions on the roof-wall edges while the discontinuous curves are linked to the diffractions followed by multiple reflections which represent the interactions between buildings or building-ground.

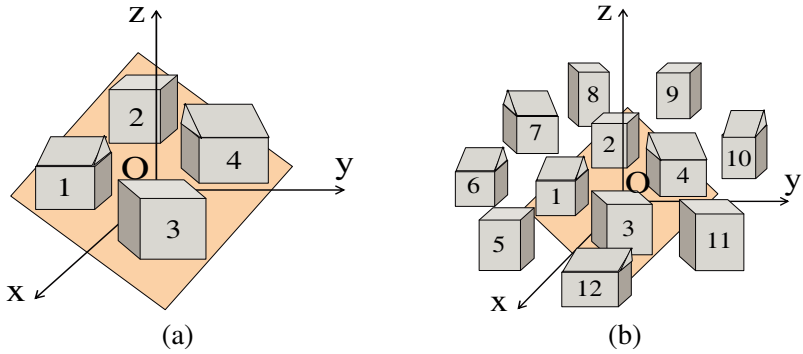

Figure 17. The configuration for a (a) four-building and (b) twelve-building area simulation.

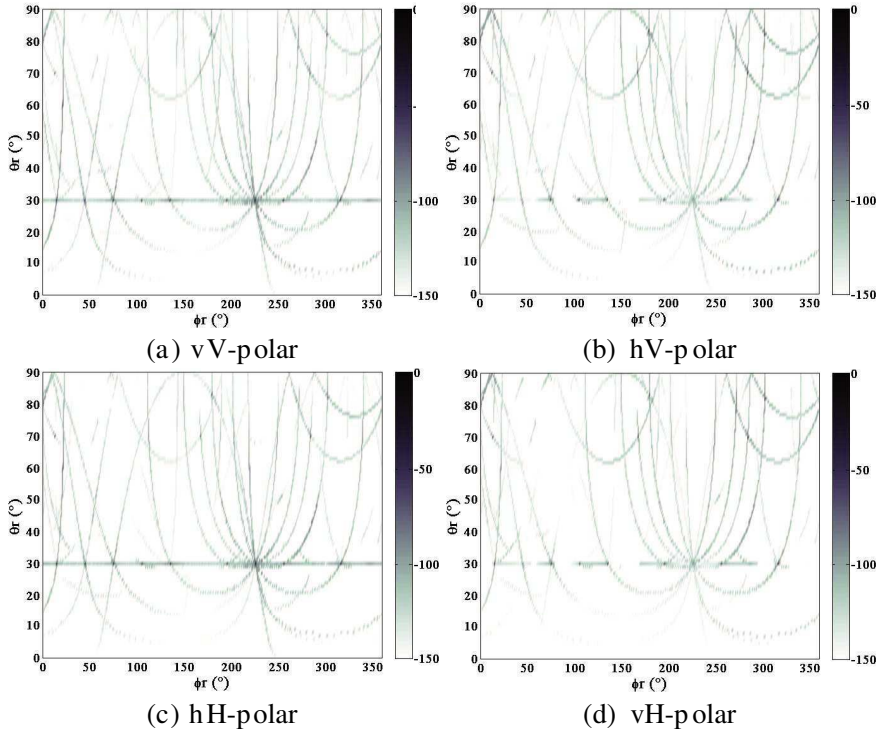

Figure 18. (a)(c) Co- and (b)(d) Cross-polar of the received field for a four-building area.

In the next simulation, let us try a more complicated configuration including twelve buildings. Beside the four buildings simulated lately, we add eight more around the illuminated zone to see the effect of these buildings on the received field. Their heights, lengths and widths are one-to-one $H = [13\ 16\ 18\ 14\ 12\ 15\ 16\ 16]$ (m), $L = [6\ 7\ 10\ 8\ 7\ 10\ 8\ 8]$ (m) and $W = [8\ 8\ 9\ 12\ 8\ 8\ 7\ 9]$ (m) (see Fig. 17(b)). The transmitter size is the same as in the previous case. We observe that when the density of buildings increases, the effects of diffractions are more considerable (see Fig. 19).

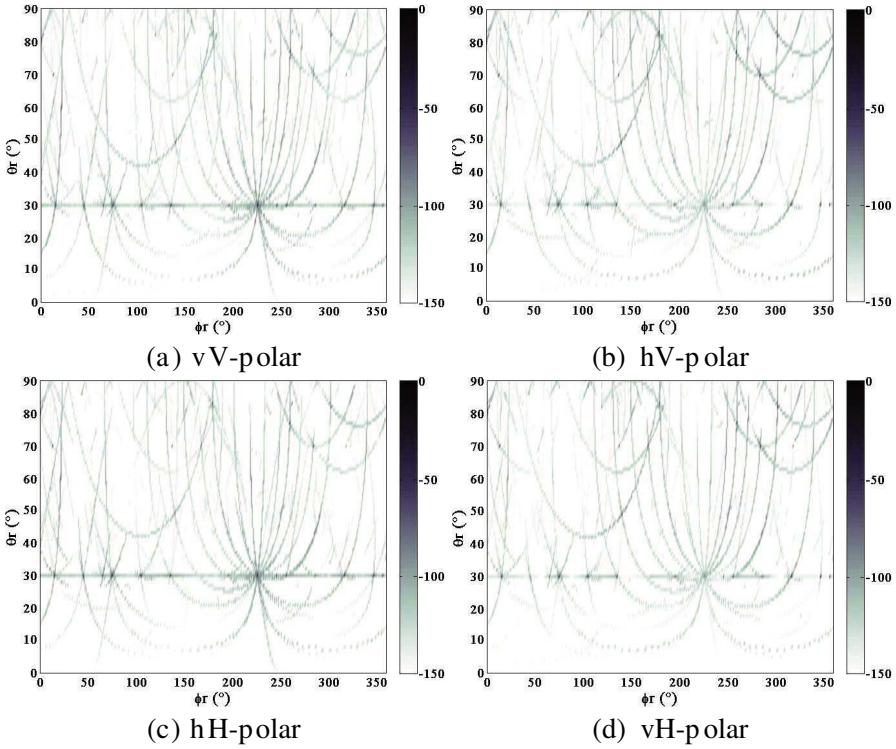

Figure 19. (a)(c) Co- and (b)(d) Cross-polar of the received field for a twelve-building area.

5. DISCUSSION

All the cases simulated previously were run on an Intel® Core(TM)2 Duo CPU, T7700 @2.40 GHz with 3.5GB of RAM. The total computation time for a single building is about one hour when we consider 500 incident rays. For a four-building area, the calculation

time goes up to six hours. Most of the CPU time is spent on finding the diffracting edges, the third-order combination ray paths related to the diffraction, such as R-R-D, R–D–R, D–R–R, etc. and higher order mechanisms. The simulation time really depends on the maximum number of interactions we choose to include.

When the ground roughness is small enough to be neglected, the dominant component of the EM scattering returns to the receiver from the group of buildings is the double-scattering (wall-ground or ground-wall mechanisms).

With regard to the dependence on the building shape, the diffraction at the edges between the roof and the walls is a crucial parameter to determine the building orientation.

With regard to the dependence on the building density, the diffraction contributes deeply to the received field.

6. CONCLUSION

We have defined a three-dimensional EM model to characterize in an efficient and accurate way the scattered field by an urban area in high-frequency range. This field depends on the polarization of the incident wave, the geometry and the materials composing of the buildings and the ground. With our model, the diffracted field by an urban area is obtained for a deterministic distribution of buildings. To obtain an average value of the diffracted field in a given direction, it should be calculated for several possible configurations and take the mean value.

In the future work, an activity is ongoing to perform more complete simulations of urban areas to include also features like building balconies, trees, cars, ... and that, from early studies, such details do not significantly contribute to the far field. This would be of much interest to the community performing parameter reconstructions from SAR data.

ACKNOWLEDGMENT

The authors would like to thank Mr Liu Weixian, Mr Feng HongChuan, Mr Sun Hongbo and Ms Xiao Yi from the Temasek Laboratories of Nanyang Technological of University (NTU), Singapore who has contributed the measurements to compare to our model. All the measurements were done in the anechoic chamber of the "ElectroMagnetic Effects Research Lab" (EMERL) of NTU on March 2010.

REFERENCES

1. Gierull, C. H., "Statistical analysis of multilook SAR interferograms for CFAR detection of ground moving targets," *IEEE Trans. on Geosci. and Remote Sens.*, Vol. 42, No. 4, 691–701, Apr. 2004.
2. Tison, C., J.-M. Nicolas, F. Tupin, and H. Maître, "New statistical model for Markovian classification of urban areas in high-resolution SAR images," *IEEE Trans. on Geosci. and Remote Sens.*, Vol. 42, No. 10, 2046–2057, Oct. 2004.
3. Garestier, F., P. Dubois-Fernandez, X. Dupuis, P. Paillou, and I. Hajnsek, "PolInSAR analysis of X-Band data over vegetated and urban areas," *IEEE Trans. on Geosci. and Remote Sens.*, Vol. 44, No. 2, 356–364, Feb. 2006.
4. De Adana, F. S., O. G/ Blanco, I. G. Diego, J. P. Arriaga, and M.F. Cátedra, "Propagation model based on ray tracing for the design of personal communication systems in indoor environments," *IEEE Trans. on Vehicular Techno.*, Vol. 49, No. 6, 2105–2112, Nov. 2000.
5. Degli-Esposti, V., "A diffuse scattering model for urban propagation prediction," *IEEE Trans. on Ant. and Propa.*, Vol. 49, No. 7, 1111–1113, Jul. 2001.
6. Chang, P. C., R. J. Burkholder, J. L. Volakis, R. J. Marhefka, and Y. Bayram, "High-frequency EM characterization of through-wall building imaging," *IEEE Trans. on Geosci. and Remote Sens.*, Vol. 47, No. 5, 1375–1387, May 2009.
7. El Sallabi, H. M. and P. Vaikikainen, "Improvements to diffraction coefficient for non-perfectly conducting wedge," *IEEE Trans. on Ant. and Propa.*, Vol. 53, No. 9, 3105–3109, Sep. 2005.
8. Soni, S. and A. Bhattacharya, "New heuristic diffraction coefficient for modeling of wireless channel," *Progress In Electromagnetics Research*, Vol. 12, 125–137, 2010.
9. XGTD®, Remcom, Inc., 2010, XGTD version 2.5.16 User's Manual.
10. Burkholder, R. J., L. J. Gupta, and J. T. Johnson, "Comparison of monostatic and bistatic radar images," *IEEE Trans. on Ant. and Propa.*, Vol. 45, No. 3, 41–50, Jun. 2003.
11. Ben Kassem, M. J. and A. Khenchaf, "Bistatic mapping radar BiSAR," *OCEANS 2003 Proceedings*, Vol. 5, 2754–2760, Sep. 2003.